Coastal Engineering 118 (2016) 50–62

Contents lists available at ScienceDirect

Coastal Engineering

journal homepage: www.elsevier.com/locate/coastaleng

Observations and modelling of nearshore sediment sorting processes along a barred beach profile

Y.B. Broekema [a,b], A. Giardino [b], J.J. van der Werf [b], A.A. van Rooijen [b], M.I. Vousdoukas [c,d,*], B.C. van Prooijen [a]

[a] Delft University of Technology, Stevinweg 1, 2628, CN, Delft, The Netherlands
[b] Deltares, Marine and Coastal Systems, P.O. Box 177, 2600, MH, Delft, The Netherlands
[c] European Commission, Joint European Research Centre (JRC), Via Enrico Fermi 2749, I-21027, Ispra, Italy
[d] Department of Marine Sciences, University of the Aegean, University hill, 41100, Mitilene, Lesbos, Greece

ARTICLE INFO

Article history:
Received 12 October 2015
Received in revised form 7 June 2016
Accepted 23 August 2016
Available online 16 September 2016

Keywords:
Sediment sorting
Bar morphology
Delft3D
Nearshore
Infragravity waves
Sediment transport
GWK Hannover

ABSTRACT

The understanding of cross-shore sediment sorting is of primary importance for the design of sand nourishments and for assessing the suitability of the seabed to different ecological species. In this paper, sediment sorting processes were investigated by using a combination of physical and detailed numerical modelling. Data from large-scale wave flume experiments were used to validate a 2DV cross-shore Delft3D model. The model solves coupled short-wave averaged equations for flow, sediment transport, bed composition and bed level change. The infra-gravity wave motions were explicitly resolved. In order to investigate sorting processes, eight sediment fractions were used as well as a layered bed stratigraphy. The effects of different wave conditions (high energetic and more moderate energetic waves) on the morphodynamic profile development and sorting processes were investigated. The Delft3D model reproduced the profile development and bar position very accurately. Additionally, model predictions of sediment sorting across the profile fitted very well with the available observations. The numerical model simulations showed the importance of including short-wave grouping and infragravity wave effects in order to reproduce the cross-shore profile development, especially the breaker bar dynamics and sediment sorting processes. Infragravity waves contribute to larger sediment entrainment and more offshore bar development. Besides leading to a better prediction of the bed profile, infragravity waves also lead to a better prediction of the bed composition. Model results are in agreement with experimental data, showing its capabilities in functioning as a tool to predict sorting processes.

1. Introduction

The sediment on natural beaches is not uniform, but shows a large spatial grain size variability. Cross-shore sediment sorting occurs due to the dependency of sediment transport on the local hydrodynamic conditions and the grain size of the available sediment. The heterogeneity in grain size may play an important role in the morphological development of the nearshore region of sandy beaches. Therefore, the understanding of the cross-shore sediment sorting is of primary importance, for example, for the design and construction of sand nourishments with a different grain size distribution with respect to the native beach.

Despite the known non-uniformity of natural beaches, coastal engineering models like Delft3D often assume for simplicity a uniform grain size for the prediction of beach and nearshore morphodynamics (e.g. Ruessink et al., 2007; Van Rijn et al., 2011). We hypothesize that taking into account sediment variability and sorting processes will impact the modelled morphodynamics.

Sorting of sediment is dependent on a combination of both sediment characteristics (size, shape and density) and hydrodynamic conditions. Slingerland and Smith (1986) distinguished two different hydraulic sorting mechanisms. First, suspension sorting involves separation of heavy from light materials according to their settling velocities and takes place during deposition. Second, entrainment sorting takes place during erosion and involves separation of grains according to their relative entrainment thresholds, usually expressed in terms of a critical bed shear stress (Komar and Wang, 1984).

Most of the existing studies on sediment sorting are based on field data. In general, an inverse depth dependency is found to the cross-shore grain size distribution, with several researchers mentioning a fining trend offshore. Van Rijn (1998) showed through a modelling study that fine sediments are transported seaward during periods of high wave energy. Stauble (1992) presented results from a long-term morphological study at the Field Research Facility beach at Duck, North Carolina. Although small variations occurred, a persistent pattern

* Corresponding author at: European Commission, Joint European Research Centre (JRC), Via Enrico Fermi 2749, I-21027, Ispra, Italy.
E-mail addresses: Y.B.Broekema@tudelft.nl (Y.B. Broekema), michalis.vousdoukas@jrc.ec.europa.eu (M.I. Vousdoukas).

http://dx.doi.org/10.1016/j.coastaleng.2016.08.009
0378-3839/

was found over time with sediment fining offshore up to the depth of closure. In addition to the fining trend, it was also mentioned by Van Rijn (1998) that coarser sediments are found around the bar area. Antia (1993) observed this as well at the shoreface of Spiekeroog (one of the southern North Sea barrier islands along the Dutch and German coast), where coarser sediments tend to occur in the bar troughs. In this multiple bar system, finer sediments where found on top of the bar.

A disadvantage of field data is that opposed to laboratory data, field conditions cannot be controlled and the measurements are generally less accurate (Van Rijn et al., 2013). In this study, cross-shore sorting processes along a profile have been investigated using a combination of data from physical experiments, where sediment samples were collected at regular time intervals during profile development, and detailed numerical modelling.

Besides the fact that coastal engineering models assume a uniform grain size, they often use phase-averaged wave modelling approach to limit the computational time (e.g. Wenneker et al., 2011). This means that typically in engineering models intra-wave properties such as skewness and asymmetry, stokes drift and bound infragravity (IG) waves are not resolved but parameterized (Ruessink et al., 2007; Van Rijn et al., 2011; Walstra et al., 2012). This could explain why engineering models often have difficulties predicting nearshore morphodynamics (Van Rijn et al., 2013). In this study, besides sorting we will also investigate the effect of taking into account IG waves on the computed morphodynamics.

The motivation of taking IG wave effects into account is to achieve an improved prediction of the different cross-shore transport components. A correct balance of all the cross-shore transport components is crucial to determine migration of breaker bars (Van Duin et al., 2004). Besides, several researchers have shown that long waves can have a strong impact on nearshore morphodynamics (e.g. Reniers et al., 2004).

For instance, Roelvink and Stive (1989) performed a quantitative comparison of the magnitude of the contribution of several components to the total cross-shore sediment transport along the Holland Coast. One of their findings was that IG waves give an offshore directed contribution to the sediment transport. They explained this by showing that the offshore directed velocities under the trough of the IG waves are coupled with the highest short waves within a wave group and thus resulting in the highest sediment concentrations. This was also found by Deigaard et al. (1999), who showed that IG waves can enhance offshore directed transports through mathematical modelling. Wave flume experiments performed by Baldock et al. (2010) showed that the presence of wave groups and the accompanying bound IG waves generally reduce onshore transport during accretive conditions and increase offshore directed transport under erosive conditions.

In this study, the state-of-the-art engineering numerical model Delft3D (Lesser et al., 2004) will be validated using data from laboratory experiment and used to study the effect of IG waves and sorting processes on cross-shore morphodynamics. Extra attention will be paid to breaker bar dynamics as the morphological development of the profile is strickly linked to sorting processes taking place across the profile.

This paper is outlined as follows: in Section 2 the Laboratory experiments are described while the model set-up is described in Section 3. The results are described in Section 4 and discussed in Section 5. Finally, Section 6 summarizes the main conclusion from the study.

2. Laboratory observations

Physical experiments were performed in the large scale wave flume of Hannover (GWK) as part of the WISE- (Water Interface Sediment Experiment) project. The project aimed in assessing hydrodynamics, waves and sediment dynamics at different experimental facilities (by using scaling) and with the use of innovative instruments. Due to different wave paddles and associated software at the different flumes, it was decided to avoid second order generation and the use of an active absorption system. The data gathered during the experiments used for this study contain spatial and temporal information on hydrodynamics, bed level changes and grain size distribution.

2.1. Facility and instrumentation

The dimensions of the wave flume are 300 m (length) × 5 m (width) × 7 m (height). The initial bathymetry was a plain sloping, sandy profile of 1:15 slope (Fig. 1), consisting of moderately sorted, nearly symmetrical medium sand with $d_{10} = 137$ μm, $d_{50} = 300$ μm and $d_{90} = 610$ μm.

In total 17 wire-type wave gauges were deployed to measure water levels at 120 Hz at different locations in the shoaling and surf zone (Fig. 1). In the swash zone, 8 MASSA M300/95 ultrasonic sensors were installed with 2 m spacing along the cross-shore profile and 1.7 m above the mean water level to provide point measurements of the water elevation at 120 Hz. From the ultrasonic sensors IG wave height in the swash zone was determined. The sensors were installed from x = 260 m to x = 274 m. To measure bed level changes, a mechanical profiler attached to a measuring carriage was used. The profiler was computer-controlled and the accuracy of the system was approximately 10 mm. Velocities were not measured.

To determine sediment composition sediment samples were taken at several locations along the cross-shore profile. The grain size distribution of the sample was determined by sieving the sand, using 8 sieves (0.063, 0.125, 0.25, 0.5, 1, 2, 4 and 8 mm).

2.2. Experimental conditions

The hydrodynamic conditions to which the profile was subjected during the different tests are summarized in Table 1. The initial plain sloping bed was subjected to erosive waves (storm-like conditions). The resulting (barred) profile was subjected to a milder wave climate. The first case involves breaker bar formation due to high energetic erosive waves, and accompanying sorting phenomena. Under the milder waves from Case 2 erosion and sediment sorting continued, but with a slower rate.

The classification of the waves (e.g. high energetic or moderate energetic) is based on the Dean number (Ω), following Wright and Short (1984):

$$\Omega = \frac{H_s}{T_p W_s} \tag{1}$$

where H_s is the significant wave height measured near the wave board [m], T_p the peak period [s] and w_s the sediment settling velocity [m/s]. The sediment settling velocity is determined according to Van Rijn et al. (2004):

$$W_s = \frac{10\nu}{D_{50}}\left[\left(1 + \frac{0.01(s\text{-}1)g\,(0.8D_{50})^3}{\nu}\right)^{0.5} \text{-}1\right] \tag{2}$$

where $s = 2.65$ is the relative density, D_{50} is the median grain diameter [m] and ν is the kinematic viscosity [10^{-6} m^2/s]. The Dean number gives an indication on whether the response of the profile to the wave conditions will be slow (low energy, reflective) or fast (high energy, dissipative).

2.3. Methodology

Waves were generated by a wave generator. Each test case consists of several wave time series of approximately 40 min. All wave time series were generated using 1st order approximation (hence no IG waves were generated at the boundary) using a JONSWAP spectrum with spectral shape factor (γ_{JONS}) equal to 3.3. After each individual time

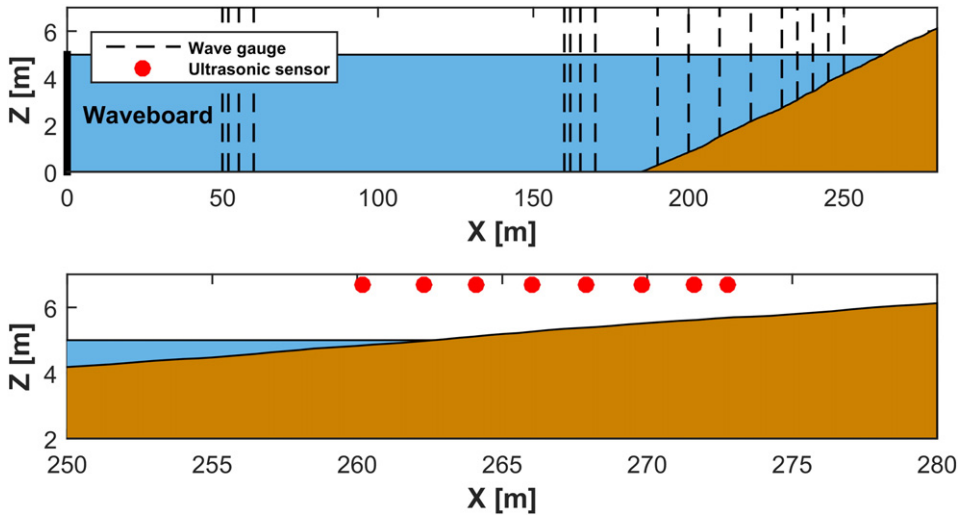

Fig. 1. Schematic overview of the experimental set-up. The upper panel shows the entire flume with the locations of the wave gauges (dashed black lines) and the lower panel zooms in on the swash-zone, where the ultrasonic sensors are installed (red dots).

series the wave paddle was stopped for 10 min after which the next time series was started.

Case 2 of the experiment was carried out directly after Case 1, meaning that the final bed profile of Case 1 is used as initial profile for Case 2. In this paper, we will refer to time equal to t_0 as the starting time of the first case, t_1 as the end of the first case and also the start of the second case, and t_2 as the end of the second case.

Bed monitoring was performed before and after each experimental run. Sediment sampling was performed at t_0, t_1 and t_2, where a volume of sand the size of a tennis ball was scraped from the surface.

Significant wave heights were determined from the zeroth-order moment of the wave spectrum. The incident-band and IG wave height were determined assuming a split frequency equal to half of the peak frequency ($f_{split} = 0.5^{*}f_{peak}$). Due to wave-wave interactions, the result of this operation is more difficult to interpret in the swash-zone, so one must be careful with drawing conclusions in this zone.

In this study, the sediment distribution is described using three parameters: the median grain diameter (D_{50}), the geometric standard deviation (σ_G) and the geometric inclusive graphic skewness (Sk_G) as given by Blott and Pye (2001).

$$\sigma_G = \exp\left(\frac{\ln(D_{84})-\ln(D_{16})}{4} + \frac{\ln(D_{95})-\ln(D_5)}{6.6}\right) \quad (3)$$

$$Sk_G = \frac{\ln(D_{16}) + \ln(D_{84})-\ln(D_{50})}{2(\ln(D_{16}) + \ln(D_{84}))} + \frac{\ln(D_5) + \ln(D_{95})-\ln(D_{50})}{2(\ln(D_5 + \ln(D_{95}))} \quad (4)$$

The standard deviation is a measure of the width of the sediment distribution. A higher standard deviation implies a more graded sample and thus a less sorted sample. Skewness measures the degree and direction of asymmetry of the distribution as well as its sign. A negative value of the skewness implies that the sediment is asymmetric towards the coarse tail of the sample and a positive value implies that the sediment is asymmetric towards the fine tail of the sample. The concepts of standard deviation and skewness as measures for sediment composition are shown in Fig. 2.

The sediment used in this study has an initial skewness of −0.05 which can be classified as nearly symmetrical following Blott and Pye

Table 1
Overview of the experiment conditions.

Test case	Test nature	H_s [m]	T_p [s]	Duration [hrs]	Dean number [−]
1	High energetic (erosive)	0.82	5.2	4.25	4.74
2	Moderate energetic (erosive)	0.62	6.3	9.00	2.95

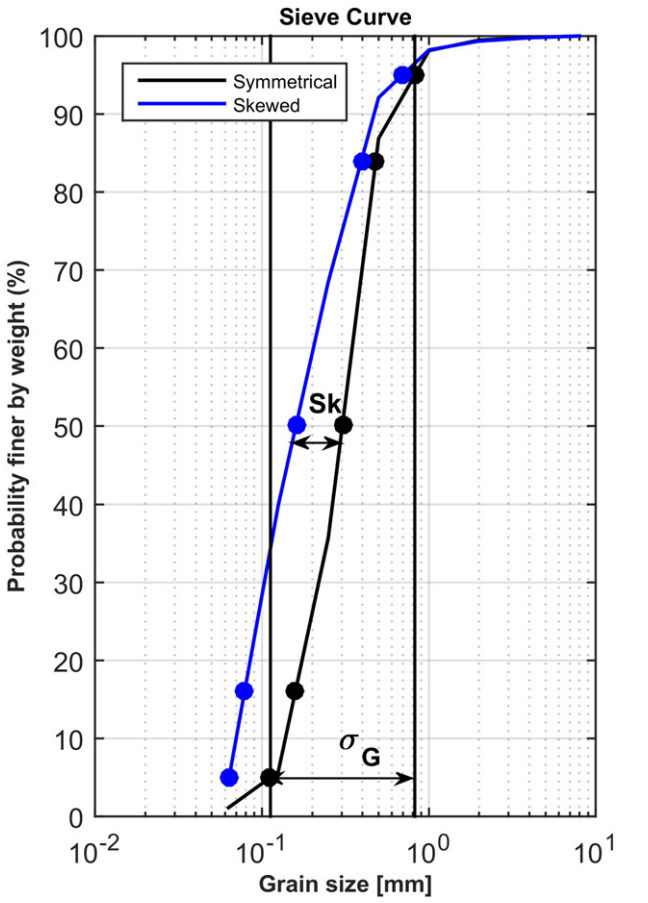

Fig. 2. Concept of standard deviation and skewness as parameters to describe sediment composition. The standard deviation (σ_G) is shown for the symmetrical curve. Skewness is illustrated as the deviation of a skewed curve from a perfectly symmetrical sample. For this example, the sieve curve is asymmetric to the fine tail.

(2001). The initial standard deviation is approximately 1.8, which is classified as moderately sorted.

3. Model set-up

The numerical modelling was performed using the Delft3D package (Lesser et al., 2004). In particular, a 2DV implementation was used to simulate the hydrodynamics, waves, sediment transport, bed composition and morphodynamics. The Delft3D morphological modelling system solves coupled short-wave averaged equations for waves, currents, sediment transport and morphological changes under the hydrostatic pressure assumption.

Analysis of the experimental data showed a clear presence of IG waves in the flume. In addition, sorting effects were also observed during the experiments. Therefore it was decided to choose the Delft3D modelling approach in which the effect of short wave grouping on long wave motions is explicitly taken into account. Furthermore, sediment transport and morphology were calculated by using multiple sediment fractions and a layered bed stratigraphy to keep track of changes in bed composition.

In the following sections, we will discuss the implementation of the wave model (Section 3.1), of the sediment transport model (Section 3.2), of the bed composition model (Section 3.3), and finally the general modelling approach (Section 3.4).

3.1. Wave model

Wave heights were computed using the roller module (Reniers et al., 2004), included in the original Delft3D-FLOW code, in a similar way as for example in other codes such as XBeach (Roelvink et al., 2009).

The Delft3D-FLOW module also solves the hydrodynamics in the model domain (horizontal momentum equations, continuity equations, transport equation, and turbulence). Contributions from wave and roller induced forces derived from gradients in the radiation stresses are added to the momentum equations. In particular, to account for the effects of short-wave groupiness on the water motion and the accompanying generation of IG waves, an instationary version of the roller model was used. In the instationary version of the roller model, time and spatial varying (on the wave group scale) wave and roller energy are used to calculate the radiation stresses, leading to time-varying hydrodynamics, swash dynamics, and sediment transports (Reniers et al., 2004). The Delft3D model has been extensively validated by for instance Lesser et al. (2004) and van Rijn et al. (2011).

For computing wave-current interactions, the hydrodynamic equations are written and solved in a GLM reference frame. Wave induced driving forces are expressed averaged over the wave period. The relationship between the GLM velocity and the Eulerian velocity is given by:

$$U = u + u_s \tag{5}$$

Where U is a GLM velocity component, u is the Eulerian velocity component and u_s is the Stokes' drift component, corresponding to a net horizontal displacement of fluid in the direction of wave propagation (Walstra et al., 2000). The Stokes drift, which is computed in the model from wave theory, is due to the fact that the wave crest moves slightly faster in forward direction then it does in backward direction. The wave-induced mass fluxes are found by integrating the Stokes drift component over the wave-averaged total water depth and compensated, for continuity, by an offshore directed current at the bed: the undertow. This implementation was extensively validated by Walstra et al. (2000).

A frequency direction energy density wave spectrum, $E(f,\theta)$, is applied at the boundary. The incident-band wave spectrum is assumed to be narrow in both frequency and distribution. Waves are unidirectional since a wave flume experiment is considered and upon investigation the spectrum is also narrow in frequency. Following the method of Van Dongeren and Svendsen (1997), a Riemann boundary is constructed allowing reflected (free) waves to leave the domain.

The model was calibrated on the hydrodynamics (wave heights and water levels) using the wave breaker criterion (gamma) and the wave roller slope parameter (beta). The wave breaker criterion induces wave breaking when a certain wave height over water depth ratio is reached (Roelvink, 1993). The roller slope parameter determines the maximum slope of the wave surface roller and determines the rate of wave energy transferred from the waves to the surface rollers and from the rollers to the water column (Svendsen, 1984). For a more extensive background on these parameters the reader is referred to Brière et al. (2010).

The calibration procedure was as follows. First the wave propagation over the profile was assessed by varying the wave breaker criterion. Second, the roller slope parameter was varied while the effect on the mean water level was determined.

For the wave breaker criterion, using the default value provided too little dissipation for Case 1 and too much dissipation for Case 2. A possible explanation for this is that due to the more energetic wave conditions for Case 1 there is stronger grouping of waves for Case 1 than for Case 2. Research by Kaihatu and Safty (2010) shows that wave groups undergo a greater degree of dissipation than equivalent random waves. Thus, for the stronger wave grouping that appears in Case 1 the model must be provided with a stronger dissipation given by a lower value of the parameter gamma, while for Case 2 gamma had to be slightly higher.

The difference in wave grouping may also explain the difference in the wave roller slope parameter, since the transfer of wave energy from the waves to the surface roller is different.

An overview of the calibrated model parameters is given in Table 2.

3.2. Sediment transport model

Sediment transport and bed level changes were computed by using multiple sediment fractions to be able to account for sorting effects. Transports were computed using the Van Rijn (2007a, 2007b, 2007c) formulation. This method distinguishes between transport below a certain reference height, a, which is treated as bed load transport and that above the reference height which is treated as suspended load transport. Sediment is entrained in the water column by imposing a reference concentration (C_a) at the reference height a. The reference concentration is, amongst other things, dependent on the bed shear stress due to currents and waves (Van Rijn, 2007b).

The computed sediment transport contains four contributions: 1) current related bedload transport, 2) wave related bedload transport, 3) current related suspended load transport and 4) wave related suspended load transport. These contributions can be scaled using f_{bed}, $f_{bed,w}$, f_{sus}, and $f_{sus,w}$ respectively.

In order to simulate multiple sediment fractions, the original sieve curve was divided into several fractions of different size. For each

Table 2
Overview of the settings of the free parameters for the calibrated model for the two cases.

Parameter	Symbol	Calibrated values	
		Case 1	Case 2
Wave breaker parameter	γ_w	0.48	0.65
Wave roller slope	β_{rol}	0.08	0.09
Suspended load current scaling	f_{sus}	0.6	0.4
Suspended load wave scaling	$f_{sus,w}$	0.05	0.05
Bed load current scaling	f_{bed}	0.25	0.25
Bed load wave scaling	$f_{bed,w}$	0.25	0.25
Longitudinal bed slope	α_{bs}	4.0	5.0
Active layer thickness	*ThTrLyr*	0.01 [m]	0.01 [m]

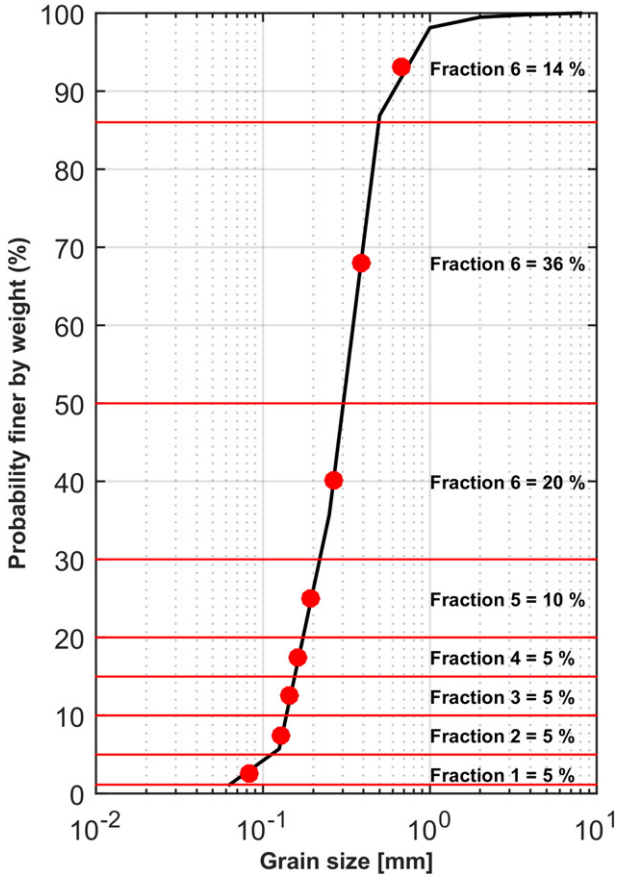

Fig. 3. Division of the original sediment sample in eight sediment fractions. Each fraction is bordered by a minimum and maximum value, indicated by the red lines. In addition to the minimum and maximum values, a median diameter per fraction is specified (red dots).

fraction the median diameter ($D_{50}^{(l)}$) and a maximum and minimum grain diameter ($D_{\min}{}^{(l)}$ & $D_{\max}{}^{(l)}$) were provided. The minimum and maximum grain diameters per fraction were determined to prevent overlap of grain sizes between different fractions. The division of the original sieve curve in different fractions is shown in Fig. 3. For this study, a total number of eight fractions was used with a higher resolution at the fine tail of the sample. The model calculates transports for each fraction separately. Bed level changes were calculated by a mass balance, where contributions for each separate fraction were simply added up. A correction factor was applied to determine the transport for each fraction, to take into account hiding/exposure effects. For this end the hiding/exposure factor of Egiazaroff (1965) was used.

The sediment transport model was calibrated by comparing measured and computed profile development. The suspended and bed load transport was calibrated individually. First, the suspended sediment transport was calibrated using the current suspended load scaling factor. This parameter was most important in determining the correct profile development. To optimize the computed morphological development we also scaled the wave related suspended load scaling factor, as well as the current and wave related bed load scaling factors. Scaling of these factors was performed based on the study of (Giardino et al., 2011) and mainly led to a more precise computation of the shape of the bar.

Compared to the studies of Brière and Walstra (2006) and Ruessink et al. (2007) the values used in this study are somewhat on the low side. However, the conditions investigated in those studies were quite different and mainly referred to field studies.

3.3. Bed composition model

The bed can be modelled as a uniform, well-mixed bed consisting of one single layer of sediment, or using a layered bed stratigraphy (e.g. Sloff et al., 2013). Using a layered bed stratigraphy allows to keep track of changes in the sediment composition while the change in sediment composition will also affect the morphological evolution.

In case of a layered bed stratigraphy, the bed is divided into several layers. The first top layer is the transport layer with a pre-defined thickness. Underneath the transport layer we have a user-defined number of underlayers. In case of erosion, sediment is supplied from the underlayers to the transport layer. In case of deposition, sediment is supplied from the transport layer and stored in the underlayers. So, the transport layer has a distributing function. Finally, the lowest layer is called the base layer. All information that does not fit in the underlayers is stored in the base layer. This could happen for example in the case that the maximum number of underlayers is reached due to accretion. For additional information, the reader is referred to Broekema (2015).

Calibration of the bed composition was performed by changing the active layer thickness. For the simulations, a constant active layer thickness was chosen within the entire domain. Analysis showed that optimal results were obtained for a thickness of 0.01 m. An overview of the calibrated model parameters and their settings is given in Table 2. More information on the calibration process can be found in Broekema (2015). Our strategy was to calibrate Case 1 and Case 2 separately, in order to achieve the best possible agreement with the experimental data. The fact that the optimal calibration parameter values differ between the two cases indicates that some of the physical processes are not included in the model and therefore this needs to be account for during calibration. With case-dependent settings, we correct for this, which allows us to study the effect of long waves and sediment sorting processes with an optimal model set-up.

3.4. Model approach

We used a 2DV model in Delft3D to represent the wave flume. The model has a width of 5 m (one grid cell), and the total length of the model equals 280 m. The size of the grid cells is variable along the x-direction with a grid size ranging between 2.0 m at the offshore boundary and 0.7 m in the nearshore area, where higher resolution is required.

The vertical resolution is described by σ-layers, each representing a constant percentage of the total water depth. The layer distribution in the z-direction is such that there is a high resolution near the bottom as well as at the surface. From bottom to surface, the layer distribution is [2, 3.2, 5, 7.9, 12.4, 19.6, 19.6, 12.4, 7.9, 5, 3.2, 1.8] % of the water depth.

There is one open boundary used, situated at the far left of the model domain ($x = 0$ m, see Fig. 1). The open boundary represents the wave board of the GWK; this means that at the boundary a wave condition is prescribed as described in Section 3.1 and following the conditions specified in Table 1.

For Case 1 the initial bathymetry is the bathymetry measured at $T = t_0$. The experiments are performed directly after each other. However, for Case 2 in the experiments, the initial bathymetry is the bathymetry measured at $T = t_1$. We used this bathymetry instead of the modelled bathymetry at $T = t_1$ to start both computational cases with a consistent bathymetry. For the initial bed composition of Case 1 we used the measured bed composition of $T = t_0$. For the initial bed composition of Case 2 we used the measured bed composition of $T = t_1$.

Model performance is rated by using the Brier Skill Score (BSS), computed according to van Rijn et al. (2003):

$$BSS = 1 - \frac{\left\langle \left(|Z_{b,c} - Z_{b,m}| - \Delta Z_{b,m} \right)^2 \right\rangle}{\left\langle \left(Z_{b,0} - Z_{b,m} \right)^2 \right\rangle} \tag{6}$$

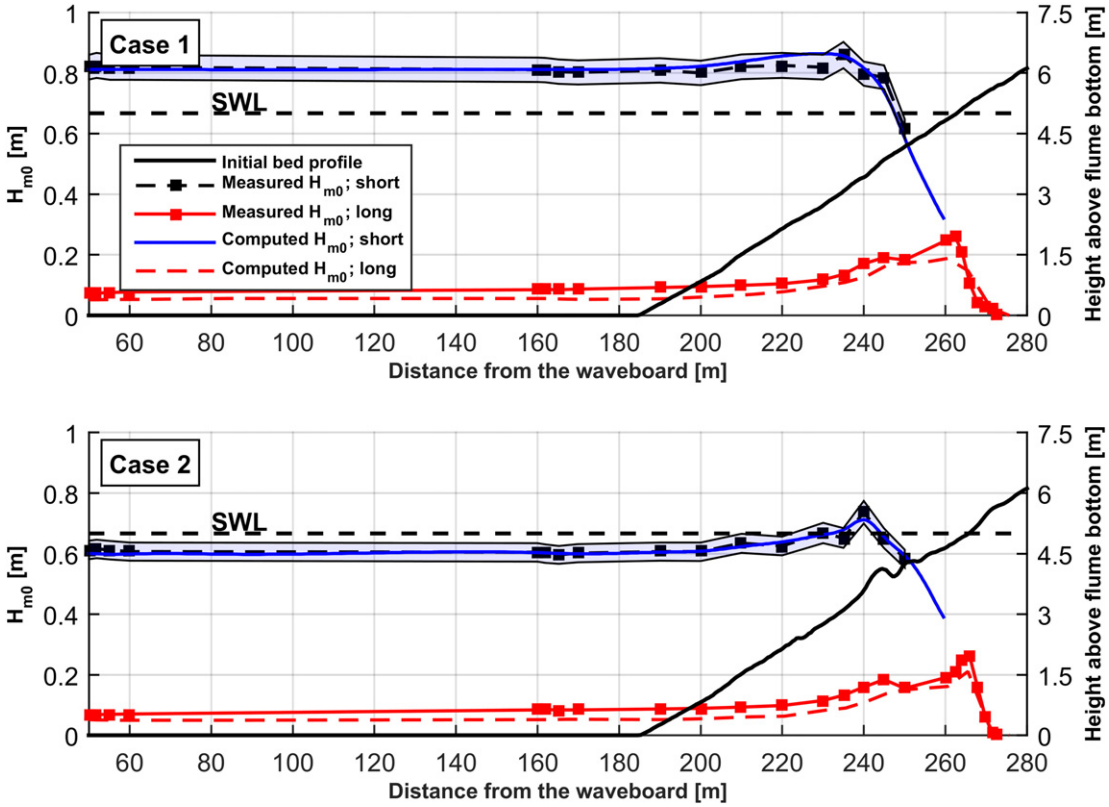

Fig. 4. Modelled and measured incident and infragravity wave height over the profile for Case 1 (upper panel) and Case 2 (lower panel). The light coloured blue area denotes ± 5% accuracy of the measured wave height.

where $z_{b,c}$ is the computed bed level, $z_{b,m}$ is the measured bed level, $\Delta z_{b,m}$ is the error in the measured bed level and $z_{b,0}$ is the initial bed level. The error in the measured bed level is given by the accuracy of the bed profiler (10 mm).

4. Results

4.1. Wave height

Fig. 4 compares measured and modelled wave heights for the high energy wave case, where the waves are split into their incident and infragravity components. For both cases a clear shoaling zone is observed with increasing wave heights followed by a wave breaking zone where the wave heights reduce at the upper part of the beach. The shoaling zone is slightly more pronounced for Case 2 as the wave period is larger. For both cases, along the entire flume IG wave height is approximately 10% of the incident wave height while this ratio increases in the surf zone. The long waves shoal in the inner surfzone.

Significant wave heights are computed accurately by the model for both cases. All computed values fall within a 5% error margin (light blue area) of the measurements.

For Case 1, the largest deviations between model and experiment are found just offshore of the breaking point, where the model predicts higher wave heights than the measurements. The wave height at the breakpoint is computed correctly and the wave breaking is modelled accurately.

The measured IG wave height across the profile is also represented reasonably well by the model. The shoaling process and the location of the maximum IG wave height are computed correctly. However, there is a difference, which is consistent across the flume, between the magnitude of the measured and computed long wave height. This is attributed to partial reflection of outgoing long waves in the wave flume while a Riemann-type of boundary is used in the model in order to damp out reflection.

For Case 2, the model shows very good agreement with the measurements in the shoaling and breaking zone, with a slight underestimation of the peak in wave height after shoaling. IG waves are again computed in accordance with the measurements, though the amplitude is smaller across the entire domain. The location of the maximum IG wave height is predicted correctly by the model.

4.2. Morphological development

Simulated and observed morphological changes for Case 1 and Case 2 are shown in Fig. 5. Clear changes to the profile, in response to the wave activity, are visible both in the measured and modelled profile. The most accurate representation as possible of the profile and breaker bar development is a very important requirement to be able to study the hydrodynamics and wave conditions along the profile which in turn affects the sorting processes.

4.2.1. Observed morphological development

Measured profiles of Case 1 show erosion high up in the profile (x = 255–270 m); the eroded sand is deposited further offshore, forming a breaker bar approximately at position x = 245 m. Besides the clear primary bar, a trough (x = 248 m) and a smaller secondary bar (x = 250 m) can be seen in the measured profile at the end of the test.

Analysis of Case 2 shows that there is a continuation of the upper shoreface erosion under the milder wave conditions, but at a much smaller rate. The eroded sand is deposited around the bar area. The measurements show that the primary bar stays approximately at the same location but grows in volume with sand deposited particularly at the offshore side of the breaker bar. Moreover, the secondary bar moves somewhat offshore and grows in height.

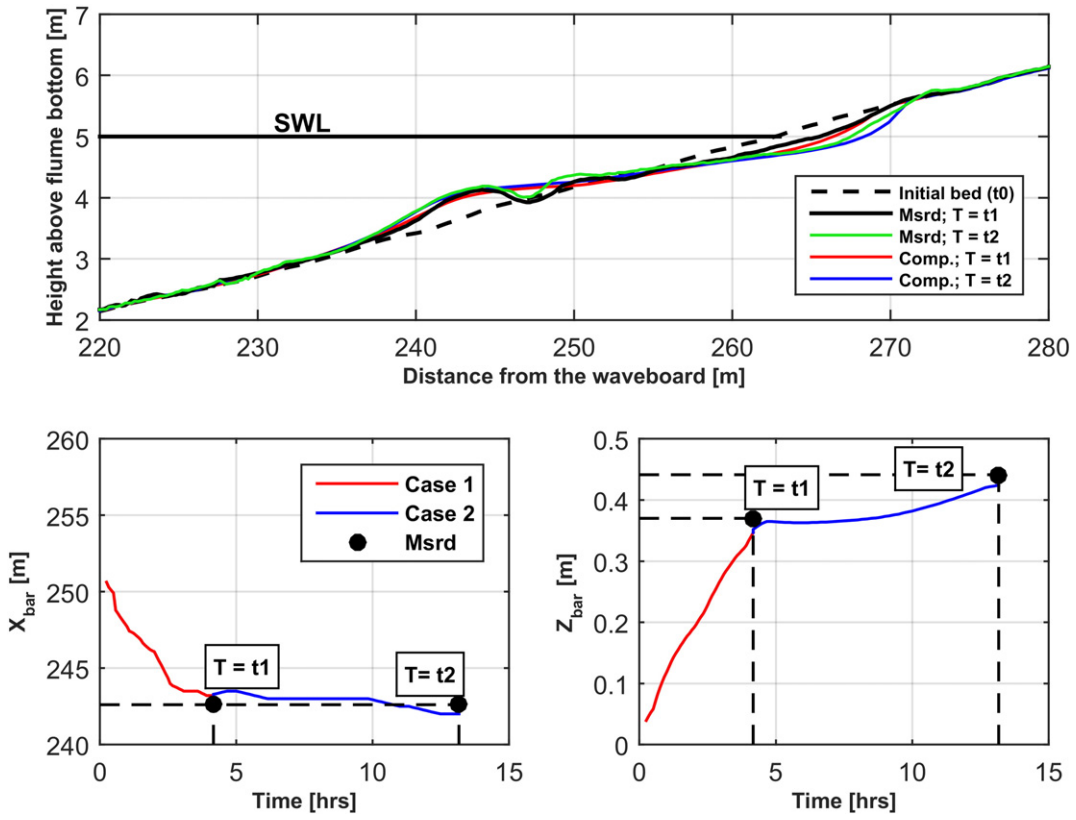

Fig. 5. Morphological development for Case 1 and Case 2. The upper panel shows the bed profiles, where measured bed profiles are given by the black ($T = t_1$) and green ($T = t_2$) lines. The computed profiles at $T = t_1$ is given by the red line and computed profile at $T = t_2$ is given by the blue line. The lower panels show the primary bar position (left) and bar height (right) development for Case 1 (red) and Case 2 (blue). Measured values at T = t1 and T = t2 are indicated by the black dots, while the development of bar position and bar height are indicated by the red and blue lines.

4.2.2. Computed morphological development

For Case 1, results from numerical modelling show that the location of the primary breaker bar is predicted very accurately by the model (Fig. 5). However, the bar trough and the secondary bar found are not reproduced by the model. The modelled erosion in the higher part of the profile is slightly overestimated with respect to the measured data. Modelled bar height and bar position are shown in detail in the lower panels of Fig. 5. The bar height was computed as the maximum deviation from the initial plane sloping bed while the bar position is taken as the position of the maximum deviation from the initial bed. The information in this part of the figure confirms the models capabilities in accurately reproducing bar height and bar position.

The Case 1 model performance is 'excellent' based on the BSS, with a BSS of 0.83 (Table 3, ISRM 8).

For Case 2, the model correctly predicts the ongoing erosion of the upper shoreface, at a smaller rate with respect to the previous high energy wave case. However, the modelled eroded volume is slightly overestimated with respect to the measurements. The overpredicted upper shoreface erosion leads to a much larger bar. The offshore bar slope is predicted accurately by the model. The trough and secondary bar are again not represented by the model.

Table 3
Brier Skill Scores for the three different model approaches for both model cases.

Model	Case 1		Case 2	
	Score	Qualification	Score	Qualification
Long waves, 8 fractions (ISRM 8)	0.83	Excellent	0.69	Good
Short waves, 8 fractions (SRM 8)	0.56	Fair	0.05	Poor
Long waves, 1 fraction (ISRM 1)	0.78	Good	0.64	Good

Modelled bar position and bar height for Case 2 compared to the measurements are also shown in Fig. 5. Offshore bar migration is slightly overestimated by the model. The figure clearly shows how the bar height is predicted very accurately by the model. In particular, the bar height is nearly stable during the first 3 h and then start growing with material eroded from the upper part of the profile. Equilibrium, in terms of the bar height, is not yet reached at the end of the simulation as the erosion of the upper part of the profile is still on-going after the 9 h of simulation. The Case 2 model performance is rated as 'good' based on the BSS, with a BSS of 0.69 (Table 3, ISRM 8).

4.3. Sorting processes

The computed changes in sediment composition are shown in Fig. 6 for both cases. The left panels show the results for Case 1 and the right panels for Case 2. The vertical distribution of the sediment in the bed as well as the surface median grain size (D_{50}), standard deviation (σ_G) and skewness (Sk_G) are shown in the figure.

4.3.1. Observed sorting processes

For Case 1 a strong fining is observed offshore of the bar crest, while a coarsening of the sediments can be seen more onshore of the bar crest. A large increase in the standard deviation offshore from the bar indicates a wider gradation of the sample which is interpreted as a settling of finer sediment fractions. This is further supported by the increase in skewness of the sediment towards a fine skewed sample. The offshore fining is explained by finer sediments staying in suspension longer than the coarser samples and settling more offshore. Coarser sediments settle around the bar area, where the undertow loses transport capacity.

Higher up in the profile, where the erosion takes place, no changes in sediment composition are observed. This implies that the wave energy

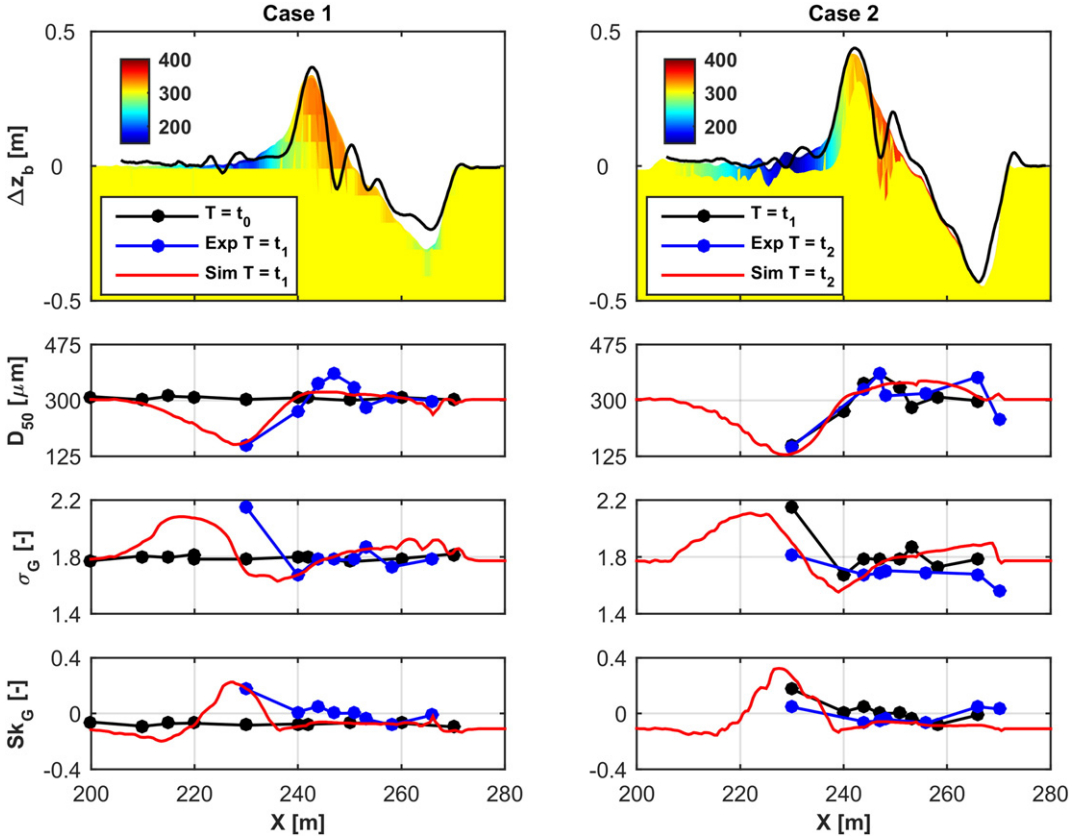

Fig. 6. Changes in sediment composition in the bed for Case 1 (left panel) and Case 2 (right panel). The upper panel shows the computed (in colours) and measured (black line) bed level changes together with the grain size distribution in the bed at the end of the simulation. The three panels below show respectively the median grain size, the standard deviation and the skewness along the flume for the initial measured data (black dotted line), the final measured data (blue dotted line) and the final computed data (red solid line).

is sufficiently high to mobilize and transport all the sediment fractions. Thus, no sorting takes place during entrainment in this area under the high energetic wave conditions. It is hypothesized that around the breaker bar some entrainment sorting takes place, meaning that the coarsening at this location is caused by a combination of settling of coarser fractions and erosion of finer fractions. However, this cannot be deduced from the experimental data.

In Case 2, the grain size offshore of the breaker bar does not change with respect to the grain size at $T = t_1$. However, the standard deviation and the skewness are slowly restoring to the initial value. This is explained by the continuous settling of sediments that are finer than the initial sand. More and more fine sand settles at the sample location, creating a thicker upper layer consisting of finer sediment, but with similar standard deviation and skewness as the original sample. This can be seen in Fig. 7 where sieve curves are plotted for t_0, t_1 and t_2 at location $x = 230$ m. A shift from the original distribution with $D_{50} = 300$ μm to a new distribution with $D_{50} = 155$ μm is observed.

For the less energetic waves in Case 2, changes in the median grain diameter higher in the profile are observed. Not all fractions are mobilized by the lower wave energy, thus leading to the observed coarsening. Waves are highly asymmetric in the inner bar region, making onshore directed bed load of coarser material an important transport mechanism. The fining around $x = 270$ m may be explained as fining onshore of the shore break through swash motions as described by Reniers et al. (2013).

4.3.2. Modelled sorting processes

For Case 1, the model predicts a coarsening of the material at the breaker bar, though the coarsening is less pronounced than in the measurements. Offshore of the breaker bar ($x = 240$ m) fining is computed by the model, in very good agreement with the observations. The change in sorting of the sample (σ_G) is also computed in the right order of magnitude, although the peak value is shifted offshore. The observed skewing of the sediment is also computed correctly by the model.

For Case 2, the model shows again an accurate representation of the offshore fining, with a slight over-prediction. A coarsening around the breaker area is computed by the model. Also a thin layer of coarse material is found in the upper part of the profile. The standard deviation is computed reasonably well by the model. However, the measurements indicate that the standard deviation is restoring more or less towards the initial state while the computations do not directly show this. The skewness is simulated reasonably well, although an asymmetry towards the fine tail is found around $x = 230$ m where the measurements give a nearly symmetrical sample.

Overall, the model is considered to provide qualitatively accurate results for the two cases investigated. The coarsening nearshore and at the bar crest and the fining trend in offshore direction were captured. Nevertheless, some local differences can be observed.

4.4. Effect of infragravity waves on morphology and sorting

To investigate the relative influence of IG waves, the simulations as described above were performed but with the roller model set to stationary mode, i.e. without the influence of IG waves so that the water level remains constant throughout the simulation. This is the common set-up in most of the engineering models. Fig. 8 shows the results of the morphodynamic bed evolution with and without accounting for the long waves. For brevity, the model accounting for IG waves is indicated as ISRM (InStationary Roller Model) to differentiate from the SRM (Stationary Roller Model) where IG waves are not accounted for.

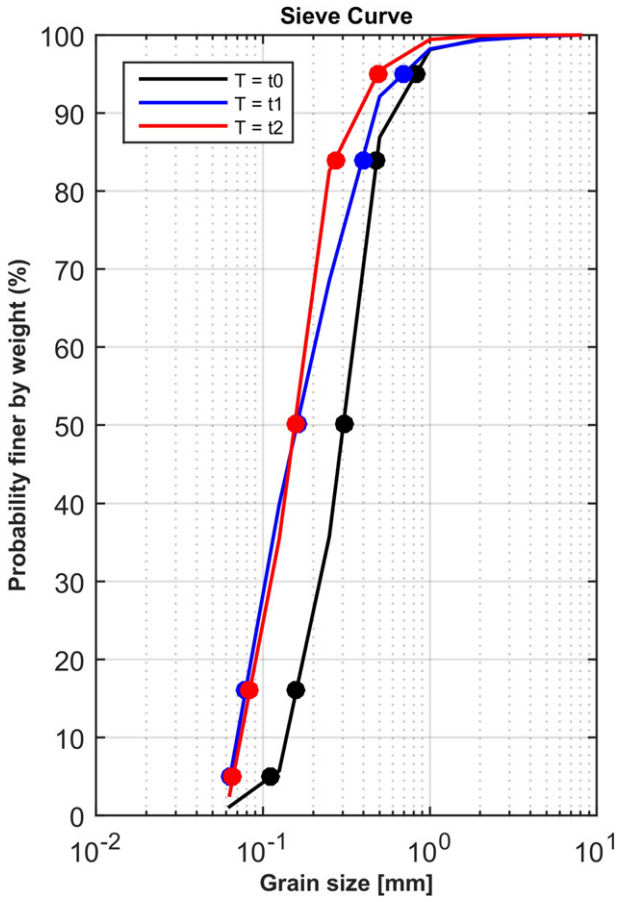

Fig. 7. Sieve curves at location X = 230 m, for times T = t_0 (black), T = t_1 (blue) and T = t_2 (red).

The upper panel of Fig. 8 shows the computed morphological profile changes for both the SRM and ISRM. A clear difference between the computed profile development can be observed. Although both model simulations give comparable beach erosion volumes, the SRM predicts the breaker bar too far onshore compared to the measurements. Also, the breaker bar height is too small in the SRM simulation (lower panels Fig. 8). The SRM performance is rated 'fair' based on the BSS, with a BSS of 0.56 (Table 3). Although not shown here, for Case 2 performance is considerably less using the SRM (rated 'poor' on the BSS, with a BSS of 0.05). This is mainly caused by an over-prediction of the upper shoreface erosion.

In order to get more insight on the effect of IG waves, the computed sediment transports along the profile have been decomposed into bed load and suspended load transport, for the two model implementations without and with IG waves (respectively SRM and ISRM). This is shown in the upper panel of Fig. 9 referring to Case 1. Although not shown, similar results were obtained for Case 2. It should be noted that suspended load transport is still the dominant transport mechanism, even though wave conditions for Case 2 are milder.

The depicted transport rates were obtained by averaging the transport rates over the first hour of simulation, when the morphological changes were small. It can be observed that, in general, the suspended load ($<q_s>$) component largely dominates the transport compared to the bed load ($<q_b>$) component. In particular, when IG waves are taken into account (ISRM), they lead to an increase of the suspended load and a decrease of the bed load in the upper part of the profile as most of the material is brought into suspension (approximately landward of X = 245 m).

The lower panels of Fig. 9 show, at different positions along the profile, the vertical distribution of the computed suspended sediment concentrations. The vertical profiles confirm that suspended transports are much larger on the higher part of the profile for the ISRM case.

We look into this in more detail by decomposing the velocity time-series and sediment concentration time-series respectively in a mean part and a fluctuating part:

$$u = \langle u \rangle + \tilde{u} \tag{7}$$
$$c = \langle c \rangle + \tilde{c} \tag{8}$$

where the symbol < > denotes the mean part, and the tilde (~) the fluctuating part on IG wave scale with respect to the averaged value. By multiplying and time-averaging the two terms in Eqs. (11) and (12), we can describe the mean suspended sediment flux as:

$$\langle uc \rangle = \langle u \rangle \langle c \rangle + \langle \tilde{u}\tilde{c} \rangle \tag{9}$$

The two terms multiplied by $\langle \tilde{u} \rangle$ and $\langle \tilde{c} \rangle$ are 0 as those two terms are null by definition. The mean suspended sediment flux computed by the ISRM, thus contains a current (mean) contribution (first term in Eq. (13)) and a long-wave mean contribution (second term in Eq. (13)). After vertical integration of the terms in Eq. (13) we obtain the net transport due to the current and long-wave variations, as shown in Fig. 10. In order to point out the relative contribution of the different terms, the transport rates have been scaled with respect to the total maximum of the sediment fluxes computed for the ISRM.

For the ISRM, we see that the current-related transport is higher, which is due to higher sediment concentrations as shown before in Fig. 9. The short-wave significant wave heights are similar for the SRM and ISRM. However, as can be seen from Fig. 4, in the inner surf zone the long waves become more important. Due to the long waves, there is more energy available to stir up sediment, leading to higher sediment concentrations. Additionally, as shown by Baldock et al. (2010), higher waves in the wave group dominate the sediment transport process because they stir up more sediment. The contribution from long waves to the total suspended transport as derived from Fig. 10 is about 20% at location X = 258 m. Higher concentrations (compared with the case with monochromatic waves) combined with higher offshore directed velocities may explain how the bar forms more offshore when the contribution from long waves is accounted for.

Simulating with or without long waves also has a large impact on computed sorting patterns. Fig. 11 shows the computed sorting derived following the SRM and ISRM approaches. The sorting patterns are directly related to the hydrodynamic forcing, sediment transport and morphological evolution of the profiles which, as shown, are quite different for the two model approaches. The model results suggest that sorting is dominated by suspended load transport moving sediment offshore. Using the ISRM leads to a larger spatial gradient in transport rates, and therefore the fining pattern found with the long wave model is much more confined compared to the short wave model.

4.5. Effect of simulating with multiple sediment fractions

To assess the relative effect of the use of multiple sediment fractions in a morphodynamic simulation versus a more standard approach with one sediment fraction only, an additional simulation was run in which instead of eight fractions only one sediment fraction was used. The sediment grain size was specified through the D_{50}, and gradation was incorporated through the D_{10} and the D_{90}. The results of this simulation are shown in Fig. 12.

The figure shows results for Case 1 only, although very similar results were obtained for Case 2. The single fraction model is indicated in the figure by $N = 1$ and the multiple fraction model is indicated by $N = 8$. As summarized in Table 3, the performance of the model with one sediment fraction is only slightly worse than the performance

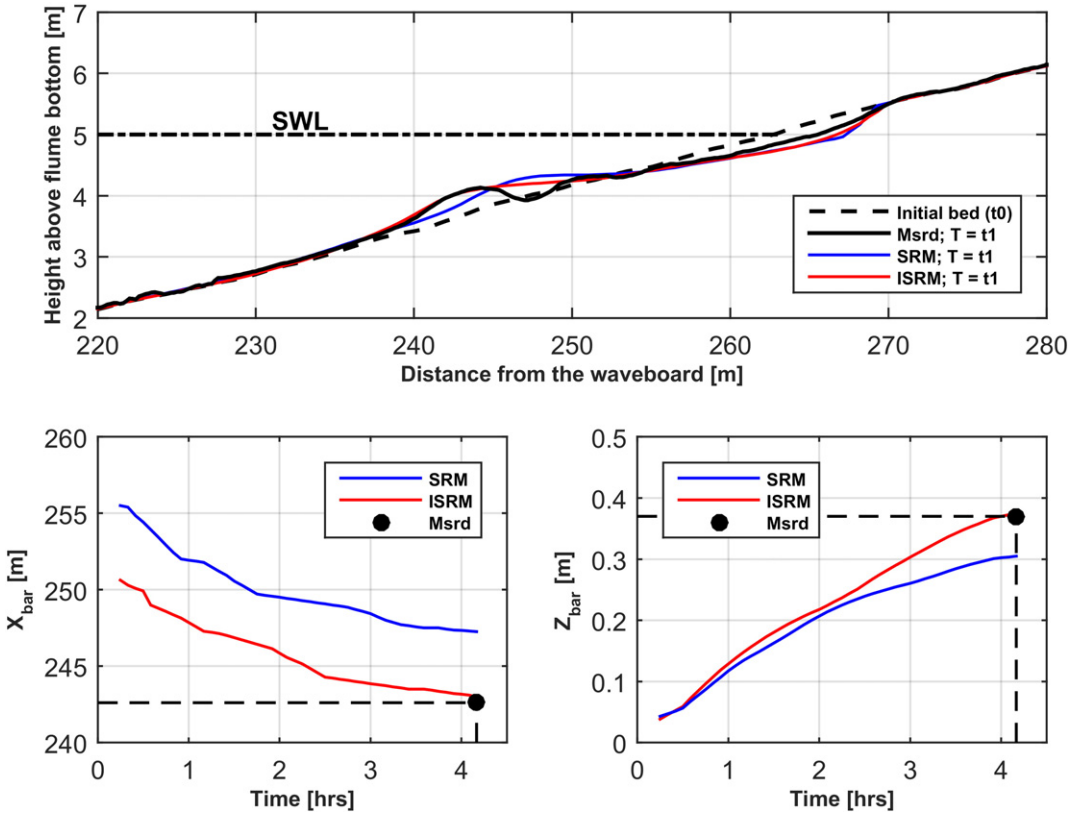

Fig. 8. Morphological development for Case 1 for the SRM and ISRM. The upper panel shows the bed profiles, where the measured bed profile at $T = t_1$ is given by the dotted black line. The profile development at $T = t_1$ following the SRM is given by the blue line and following the ISRM is given by the red line. The lower panel show the bar position (left) and bar height (right) development following the SRM (blue) and ISRM (red) approach. Measured values at $T = t_1$ are indicated by the black dots.

including eight fractions (BSS = 0.78 for N = 1 versus BSS = 0.83 for N = 8). This makes the results rating as "good" instead of "excellent". Similarly for Case 2, the BSS with N = 1 is 0.64 with respect to a BSS of 0.69 with N = 8.

The difference is mainly related to the fact that the use of eight fractions allows for a slightly better representation of the upper shoreface erosion. Moreover, the use of different fractions also leads to a slightly larger diffusion of the bar, leading to a lower bar height. Overall, based on the simulations performed in this study the effect of simulating with multiple sediment fractions seems limited. It is reasoned that this is because the transport formulations of Van Rijn (2007a, 2007b, 2007c) already take a certain kind of spreading of the sediment into account by including D_{10} and D_{90} in the equations. Furthermore, the equations were derived using large scale transport data where bulk parameters (like the median grain diameter) were used to describe the sediment composition. Also, the sediment used in this study is relatively well sorted.

5. Discussion

For clarity, discussion points have been groups under three main topics.

5.1. Model calibration

To obtain accurate results the model was calibrated through several free parameters, as summarized in Table 2. Two different cases were simulated, forced by different wave conditions; for this reason the model was recalibrated and different sets of free parameters were used for the two cases. This might seem inconvenient for engineering purposes; nevertheless, it was decided to follow this more rigorous approach in this case in order to get the best representation of the profile development for each condition. In this way, we could use the resulting model set-up to study long wave and sediment sorting effects on cross-shore profile development with a certain degree of confidence.

5.2. Morphological bar development

In Delft3D incident waves are not directly resolved. Instead, many parameterisations are used to include higher order non-linear properties such as wave asymmetry and velocity skewness (Wenneker et al., 2011). A wave-by-wave approach might yield more accurate predictions of these effects on wave-related sediment transport. Nevertheless, as Ruessink et al. (2007) noted, an incident-wave resolving approach is computationally much more expensive and not yet suitable for engineering applications. Despite this limitation our results in terms of morphological prediction of the primary bar, are already very accurate, also compared to similar studies on the same subject. The main differences, compared to other similar studies (e.g. Tonnon et al., 2009; Walstra et al., 2012), relates to the inclusion of incident wave-grouping and IG waves. Nevertheless, including IG waves did not yield improvements in predicting the bar trough formation. According to breakpoint theory, breaker bar formation occurs due to sediment transport convergence (Absalonsen, 2012). In order to have multiple bars, multiple sediment convergence points are needed. Considering the transport in our model (Fig. 9) we have only one sediment convergence point, which is the primary bar. Non-linear wave effects like wave asymmetry and velocity skewness are of primary importance to solve the inner bar-dynamics. A more detailed wave model would be required to do so. Wenneker et al. (2011) used a Boussinesq-type wave driver to drive the morphological model. In their results, multiple sediment convergence points are computed in the bar region leading to

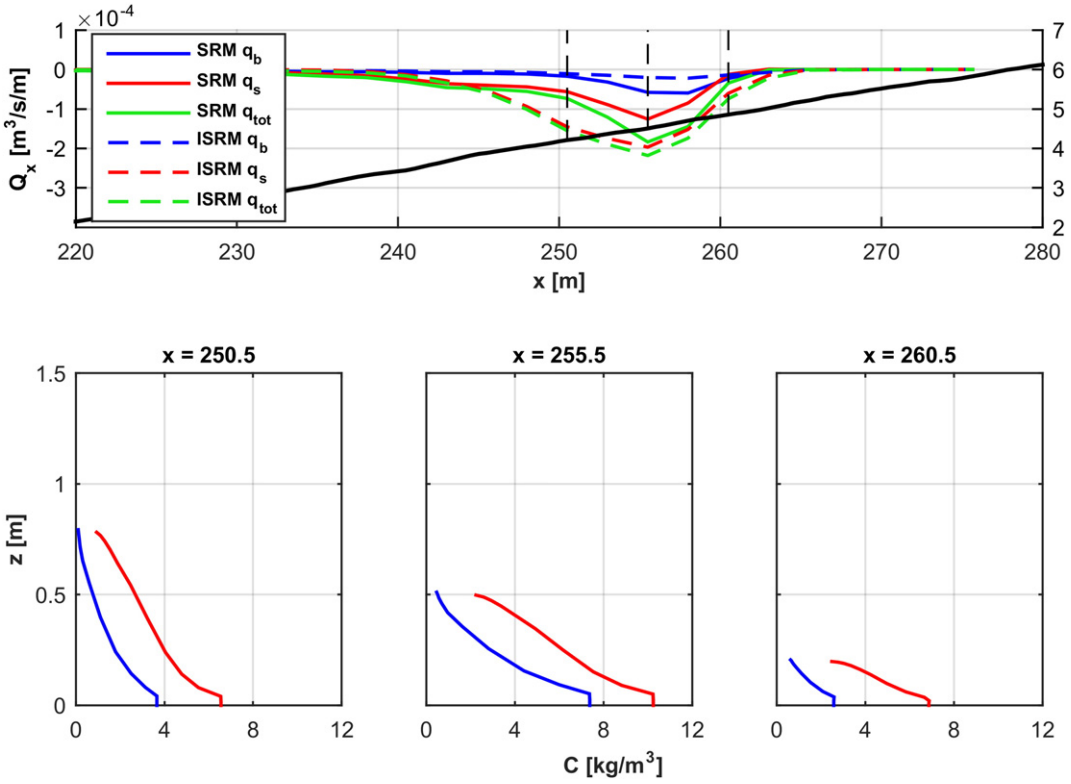

Fig. 9. Upper panel: transport rates decomposed in bed load (blue), suspended load (red) and total load (green) for both the SRM (solid line) and ISRM (dashed line). Lower panel: vertical distribution of suspended sediment concentrations for the SRM (blue) and ISRM (red) at several locations along the profile denoted by the black dotted lines in the upper right panel. The depicted transport rates and concentration profiles were obtained by averaging over the first hour of simulation, when the morphological changes were small. Results refer to Case 1.

a better description of the inner bar region. However, more research effort is needed in order to fully solve these types of morphological features (Van Rijn et al., 2013).

5.3. Effect of simulating with multiple sediment fractions

The results have shown that the use of multiple fractions does not lead to considerable improvements of the results in terms of morphodynamic representation of the profile development. However, it is important to point out that, whether the use of multiple fractions in the model is needed for a more accurate representation of the morphological profile development, also depends on the initial gradation of the sediments. In these experiments, relatively large sediment was used with moderate sorting. Nevertheless, despite the initially moderate sorting of the sediment, clear spatial sorting during the experiments and simulations was visible.

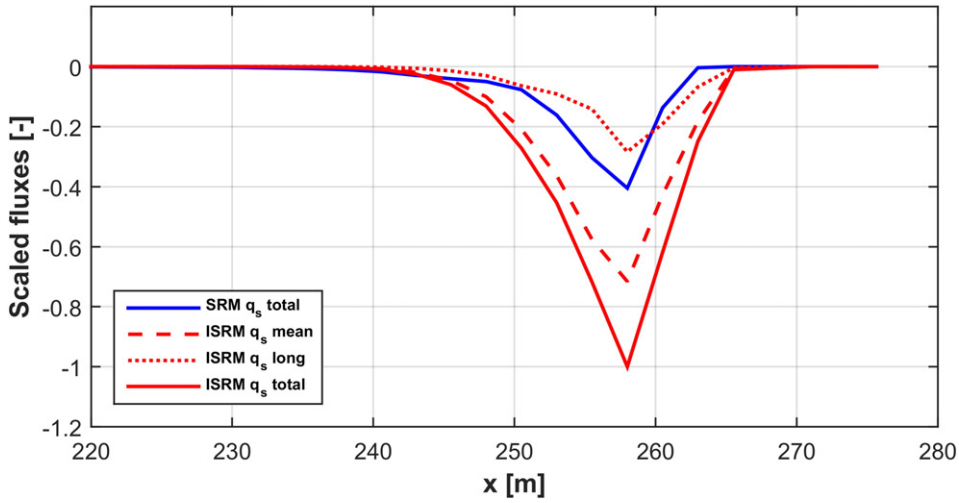

Fig. 10. Decomposed suspended sediment flux for both ISRM and SRM for Case 1. The blue line shows the total suspended transport as computed by the SRM, the red solid line the total suspended transport as computed by the ISRM, the red dashed line the mean contribution from mean velocities and mean concentrations to the sediment fluxes as computed by the ISRM, and the red dotted line the mean contribution of the fluctuating velocities and concentrations as computed by the ISRM.

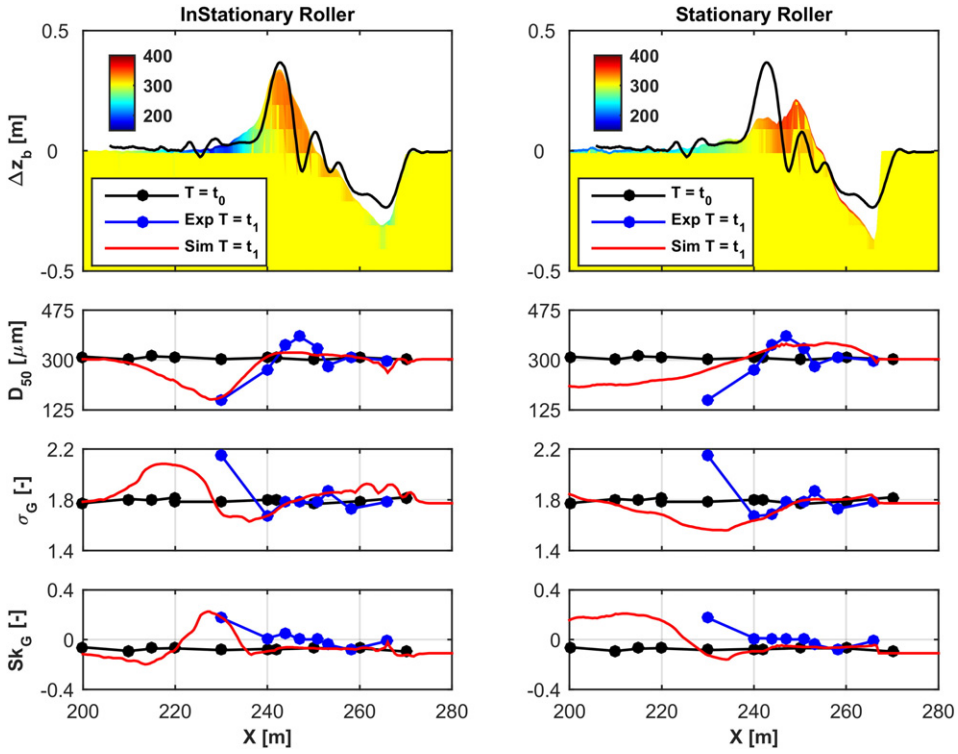

Fig. 11. Changes in sediment composition in the bed for the SRM (left panel) and ISRM (right panel) for Case 1. The upper panel shows the computed (in colours) and measured (black line) bed level changes together with the grain size distribution in the bed at the end of the simulation. The three panels below show respectively the median grain size, the standard deviation and the skewness along the flume for the initial measured data (black dotted line), the final measured data (blue dotted line) and the final computed data (red solid line).

6. Conclusions

In this paper, cross-shore morphodynamics and sediment sorting processes for a barred beach were investigated based on a combination of large-scale wave flume experiments and detailed numerical modelling using the Delft3D modelling system. The Delft3D model was implemented in 2DV mode, also including infragravity (IG) wave effects using the instationary version of the roller module of Delft3D-FLOW. Furthermore, sediment sorting processes were included by modelling eight sediment fractions and by keeping track of the bed composition with a layered bed stratigraphy.

This study focused on two test cases forced by different wave conditions (high-energetic wave conditions and moderate-energetic wave conditions, respectively Case 1 and Case 2). During Case 1 an offshore breaker bar developed, that remained approximately at the same location and with the same dimensions during the subsequent Case 2.

The measurements clearly showed the effect of sediment sorting processes along the profile. During both cases, fining offshore of the breaker bar was observed, due to fine sediments staying in suspension longer than the coarser sand and settling more offshore. At the breaker bar and more onshore of the breaker bar, sediment became coarser. Coarser sediments are more difficult to keep in suspension and as

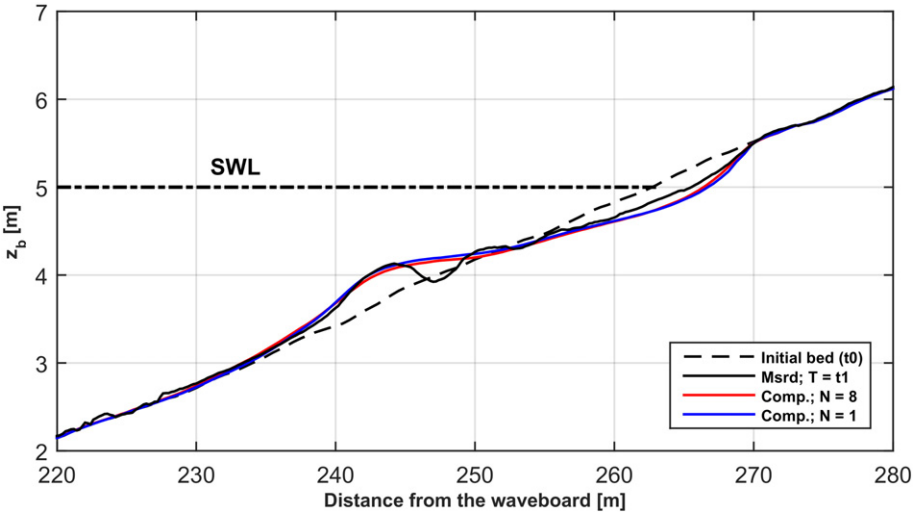

Fig. 12. Computed and measured change in bed level for Case 1. A model implementation using 8 sediment fractions ($N = 8$, red) and a model implementation using 1 sediment fraction ($N = 1$, blue) are compared to the measured changes in bed level (black, dotted).

such they settle earlier in the profile. Case 2, characterized by more moderate wave conditions, also showed coarsening higher in the profile, related to selective entrainment of the sediment bed.

The model was able to accurately reproduce the incident and IG wave transformation. Furthermore, the model captured the development of the bed level and bed composition. Erosion high in the profile was slightly overestimated by the model. The model computed accurately the breaker bar location and height which were necessary requirements for a proper prediction of the sorting processes. Sorting patterns were correctly predicted by the model: fining offshore from the breaker bar was computed accurately and coarsening around the bar area was also shown by the model, though less pronounced as observed.

This validated model was used to investigate the effect of IG waves on profile development and sediment sorting processes. The results suggest that incident wave grouping and IG waves are important for an accurate prediction of the cross-shore profile. The presence of incident wave groups and infragravity waves results in higher sediment concentrations onshore of the breaker bar as more sediment was entrained by higher waves in incident the wave groups. Furthermore, sediment was more easily transported further offshore due to maximum offshore long wave velocities which coincided with highest sediment concentrations.

Finally, the relative effect of using different sediment classes with respect to an approach with one sediment class only was assessed. Model results showed only a slight improvement in terms of profile development when eight sediment classes were used with respect to a case with one sediment class only. This for the case simulated in the physical experiments which was characterized by relatively large sand and moderate sorting.

The model implemented in this study was used to simulate laboratory experiments under controlled conditions in terms of wave conditions, morphology and sediment size. Given its ability to accurately reproduce the measured hydrodynamics and morphological profile changes, it is concluded that the model could be a very useful tool also in several field applications, including the design of nourishments or the impact of sand sorting on nearshore biology and ecology.

Acknowledgements

This research was partly funded by WVL Rijkswaterstaat, as part of the KPP-B&O Kust project. The experiments were funded from the European Community Seventh Framework Programme, under the Integrated Infrastructure Initiative Hydralab IV, Contract no. 261520. Dr. Vousdoukas acknowledges funding from the JRC exploratory research project Coastalrisk. The authors are also grateful to Matthias Kudella, Hernan Fernandez and all the other Forschungszentrum Küste staff for their invaluable support. Finally, Marcel Stive and Ad Reniers are thanked for their comments during the course of this work.

References

Absalonsen, L., 2012. Sand Bar Behaviour: Observations and Modelling. University of Florida.
Antia, E.E., 1993. Surficial grain-size statistical parameters of a North Sea shoreface-connected ridge : patterns and process implication. Geo-Mar. Lett. 13, 172–181.
Baldock, T.E., Manoonvoravong, P., Pham, K.S., 2010. Sediment transport and beach morphodynamics induced by free long waves, bound long waves and wave groups. Coast. Eng. 57, 898–916. http://dx.doi.org/10.1016/j.coastaleng.2010.05.006.
Blott, S.J., Pye, K., 2001. GRADISTAT : a grain size distribution and statistics package for the analysis of unconsolidated sediments. Earth Surf. Process. Landf. 26, 1237–1248. http://dx.doi.org/10.1002/esp.261.
Brière, C., Walstra, D.J.R., 2006. Modelling of Bar Dynamics. Report Z4099. WL|Delft Hydraulics, The Netherlands.
Brière, C., Giardino, A., van der Werf, J., 2010. Morphological modeling of bar dynamics with Delft3D: the quest for optimal free parameter settings using an automatic calibration technique. Coast. Eng. 1–12.
Broekema, Y.B., 2015. Modelling of Grain Sorting Mechanisms in the Nearshore Area for Natural and Nourished Beaches. Delft University of Technology.
Deigaard, R., Jakobsen, J.B., Fredsøe, J., 1999. Net sediment transport under wave groups and bound long waves. J. Geophys. Res. 104, 13559. http://dx.doi.org/10.1029/1999JC900072.
Egiazaroff, E.V., 1965. Calculation of non-uniform sediment concentrations. J. Hydraul. Div. ASCE 91 (HY 4).
Giardino, A., Brière, C., van der Werf, J., 2011. Morphological Modelling of Bar Dynamics with Delft3D: The Quest for Optimal Parameter Settings.
Kaihatu, J.M., Safty, H.M.E., 2010. Spectral Description of Energy Dissipation in Breaking Wave Groups. Proceedings of 32nd Conference on Coastal Engineering, Shanghai, China, 2010, pp. 1–10.
Komar, P.D., Wang, C., 1984. Processes of selective grain transport and the formation of placers on beaches. J. Geol. 637–655.
Lesser, G.R., Roelvink, J.A., van Kester, J.A.T.M., Stelling, G.S., 2004. Development and validation of a three-dimensional morphological model. Coast. Eng. 51, 883–915. http://dx.doi.org/10.1016/j.coastaleng.2004.07.014.
Reniers, A.J.H.M., Roelvink, J.A., Thornton, E.B., 2004. Morphodynamic modeling of an embayed beach under wave group forcing. J. Geophys. Res. 109, C01030. http://dx.doi.org/10.1029/2002JC001586.
Reniers, A.J.H.M., Gallagher, E.L., MacMahan, J.H., Brown, J.A., van Rooijen, A.A., van Thiel de Vries, J.S.M., van Prooijen, B.C., 2013. Observations and modeling of steep-beach grain-size variability. J. Geophys. Res. Oceans 118, 577–591. http://dx.doi.org/10.1029/2012JC008073.
Roelvink, J.A., 1993. Dissipation in random wave groups incident on a beach. Coast. Eng. 19, 127–150.
Roelvink, J.A., Stive, M.J.F., 1989. Bar-generating cross-shore flow mechanisms on a beach. J. Geophys. Res. 94, 4785–4800.
Roelvink, J.A., Reniers, A.J.H.M., van Dongeren, A.R., van Thiel de Vries, J.S.M., McCall, R.T., Lescinski, J., 2009. Modelling storm impacts on beaches, dunes and barrier islands. Coast. Eng. 56, 1133–1152. http://dx.doi.org/10.1016/j.coastaleng.2009.08.006.
Ruessink, B.G., Kuriyama, Y., Reniers, A.J.H.M., Roelvink, J.A., Walstra, D.J.R., 2007. Modeling cross-shore sandbar behavior on the timescale of weeks. J. Geophys. Res. 112, F03010. http://dx.doi.org/10.1029/2006JF000730.
Slingerland, R., Smith, N.D., 1986. Occurrence and formation of water-laid placers. Annu. Rev. Earth Planet. Sci. 14, 113–147.
Sloff, K., Van Spijk, A., Stouthamer, E., Sieben, A., 2013. Understanding and managing the morphology of branches incising into sand–clay deposits in the Dutch Rhine Delta. Int. J. Sediment Res. 28, 127–138. http://dx.doi.org/10.1016/S1001-6279(13)60025-6.
Stauble, D.K., 1992. Long Term Profile and Sediment Morphodynamics: Field Research Facility Case History. Technical Report CERC-92-7, U.S. Army Engineer Research and Development Center. Coastal and Hydraulics Laboratory, Vicksburg, MS (252 p).
Svendsen, I.A., 1984. Mass flux and undertow in a surfzone. Coast. Eng. 8, 347–365.
Tonnon, P.K., Hoyng, C.W., Van Rijn, L.C., 2009. Beach Profile Modeling at Different Scales. Coastal Dynamics.
Van Dongeren, A.R., Svendsen, I.A., 1997. Absorbing-generating boundary conditions for shallow water models. J. Waterw. Port Coast. Ocean Div. ASCE 123, 303–313.
Van Duin, M.J.P., Wiersma, N.R., Walstra, D.J.R., van Rijn, L.C., Stive, M.J.F., 2004. Nourishing the shoreface: observations and hindcasting of the Egmond case, the Netherlands. Coast. Eng. 51, 813–837. http://dx.doi.org/10.1016/j.coastaleng.2004.07.011.
Van Rijn, L.C., 1998. The Effect of Sediment Composition on Cross-Shore Bed Profiles. Coastal Engineering, pp. 2495–2508.
Van Rijn, L.C., 2007a. Unified view of sediment transport by currents and waves. I : initiation of motion, bed roughness, and bed-load transport. J. Hydraul. Eng. 133, 649–667.
Van Rijn, L.C., 2007b. Unified view of sediment transport by currents and waves. II: suspended transport. J. Hydraul. Eng. 133, 668–689. http://dx.doi.org/10.1061/(ASCE)0733-9429(2007)133:6(668).
Van Rijn, L.C., 2007c. Unified view of sediment transport by currents and waves. III: graded beds. J. Hydraul. Eng. 133, 761–765.
Van Rijn, L.C., Walstra, D.J.R., Grasmeijer, B., Sutherland, J., Pan, S., Sierra, J.P., 2003. The predictability of cross-shore bed evolution of sandy beaches at the time scale of storms and seasons using process-based profile models. Coast. Eng. 47, 295–327. http://dx.doi.org/10.1016/S0378-3839(02)00120-5.
Van Rijn, L.C., Walstra, D.J.R., Van Ormondt, M., 2004. Description of TRANSPOR2004 and Implementation in Delft3D-ONLINE.
Van Rijn, L.C., Tonnon, P.K., Walstra, D.J.R., 2011. Numerical modelling of erosion and accretion of plane sloping beaches at different scales. Coast. Eng. 58, 637–655. http://dx.doi.org/10.1016/j.coastaleng.2011.01.009.
Van Rijn, L.C., Ribberink, J.S., Van Der Werf, J., Walstra, D.J.R., 2013. Coastal sediment dynamics: recent advances and future research needs. J. Hydraul. Res. 51, 475–493. http://dx.doi.org/10.1080/00221686.2013.849297.
Walstra, D.J.R., Roelvink, J.A., Groeneweg, J., 2000. Calculation of wave-driven currents in a 3D mean flow model. Coast. Eng. 2000 (40549), 1050–1063. http://dx.doi.org/10.1061/40549(276)81.
Walstra, D.J.R., Reniers, A.J.H.M., Ranasinghe, R., Roelvink, J.A., Ruessink, B.G., 2012. On bar growth and decay during interannual net offshore migration. Coast. Eng. 60, 190–200. http://dx.doi.org/10.1016/j.coastaleng.2011.10.002.
Wenneker, I., van Dongeren, A., Lescinski, J., Roelvink, D., Borsboom, M., 2011. A Boussinesq-type wave driver for a morphodynamical model to predict short-term morphology. Coast. Eng. 58, 66–84. http://dx.doi.org/10.1016/j.coastaleng.2010.08.007.
Wright, L.D., Short, A.D., 1984. Morphodynamic variability of surf zones and beaches: a synthesis. Mar. Geol. 56, 93–118.